Extending a Macro-Element Approach for the Modeling of 3D Masonry Structures Under Transient Dynamic Loading

Damien Decret, Yann Malecot, Yannick Sieffert, Florent Vieux-Champagne, Laurent Daudeville

applied sciences

MDPI

Article

Extending a Macro-Element Approach for the Modeling of 3D Masonry Structures Under Transient Dynamic Loading

Damien Decret, Yann Malecot, Yannick Sieffert, Florent Vieux-Champagne and Laurent Daudeville *

Univ. Grenoble Alpes, CNRS, Grenoble INP, 3SR, 38000 Grenoble, France;
ddecret@bsin.k12.nm.us (D.D.); yann.malecot@univ-grenoble-alpes.fr (Y.M.);
yannick.sieffert@univ-grenoble-alpes.fr (Y.S.); florent.vieux-champagne@univ-grenoble-alpes.fr (F.V.-C.)
* Correspondence: laurent.daudeville@univ-grenoble-alpes.fr

Abstract: Masonry structures, particularly those used in developing countries and in historic buildings, typically consist of unreinforced masonry (URM) walls connected by timber or reinforced concrete elements. This study proposes enhancements to the existing two-dimensional (2D) deformable frame model (DFM) to enhance its ability in simulating masonry walls with a specific focus on accurately predicting the transient dynamic response of three-dimensional (3D) masonry structures while maintaining a minimal number of degrees of freedom (DOF). For the modeling of URM walls, the DFM framework employs elastic beams and diagonal struts with nonlinear constitutive behavior. Structural elements, such as reinforced concrete or timber reinforcements, are represented using conventional beam finite elements. This paper first reviewed the current DFM configuration, which primarily addresses the in-plane (IP) behavior of URM structures. It then introduced modifications tailored for 3D structural analysis. The reliability of the enhanced model was validated through two approaches. First, a modal analysis compared the results from the updated DFM with those from a reference 3D model based on cubic finite elements. Second, a shaking table experiment conducted on a half-scale masonry house was simulated. The findings demonstrate that, despite its limited number of DOF, the updated DFM effectively captures the main natural vibration modes. Furthermore, it shows the model's ability to predict the nonlinear transient dynamic response of 3D masonry structures with accuracy and limited computational time.

Keywords: 3D macro model; finite element method; unreinforced masonry; modal analysis; nonlinear transient dynamics analysis; in-plane and out-of-plane loadings

Citation: Decret, D.; Malecot, Y.; Sieffert, Y.; Vieux-Champagne, F.; Daudeville, L. Extending a Macro-Element Approach for the Modeling of 3D Masonry Structures Under Transient Dynamic Loading. *Appl. Sci.* **2024**, *14*, 11080. https://doi.org/10.3390/app142311080

Academic Editor: Dario De Domenico

Received: 28 October 2024
Revised: 22 November 2024
Accepted: 26 November 2024
Published: 28 November 2024

1. Introduction

Analyzing 3D masonry structures under dynamic loads is highly demanding in terms of time and computational resources, mainly due to the complex dissipative behaviors of masonry walls. This complexity necessitates 3D nonlinear transient dynamic analyses, which are both sophisticated and resource-intensive. For instance, Valente conducted, in 2022, 3D nonlinear dynamic analyses on two historical fortified masonry palaces using 455,000 and 345,000 four-node tetrahedral finite elements (FE) [1]. Similarly, in 2023, Valente performed analyses on two masonry churches with 266,000 and 145,000 FE [2]. These recent studies are notable as they enabled nonlinear dynamic analyses of complex historical structures; however, the computational demands constrained the refinement of discretization, and this limitation resulted in a FE size ranging between 20 cm and 40 cm, which is comparable to the characteristic dimensions of the masonry elements. In addition, these FE analyses were carried out using the software code Abaqus [3], which requires complex developments to implement constitutive laws specific to masonry in user subroutines. Consequently, employing a simplified model based on a macro-element with nonlinear constitutive behavior appears particularly relevant, especially for the seismic analysis of large complex masonry constructions.

To address these challenges, researchers have developed various modeling techniques specifically designed for masonry structures, especially infill walls made of unreinforced masonry (URM). These innovative methods aim to optimize the analytical process by preserving critical insights into structural behavior while significantly reducing computational time.

Among the different proposed strategies, the pier/spandrel partition is the most common, also known as the equivalent frame model (EFM) [4–9], which is recommended by international standards such as Eurocode 8 [10] or FEMA 356 [11] (Federal Emergency Management Agency). Although these models have been used to simulate complex structures, they mainly focus on determining the in-plane (IP) behavior of the structure. Only a few studies have proposed the determination of out-of-plane (OOP) behavior [12]; these studies model the OOP behavior using a strategy similar to that of the IP direction, with adjusted values for the parameters.

Another significant advancement in 3D URM structural modeling involves the integration of the rigid body spring model (RBSM) and the rigid element model (REM) [13–16]. These models consist of rigid elements interconnected through a combination of springs to simulate IP behavior or hinges for OOP behavior. These springs and hinges are characterized by their inelastic behavior, and they are defined by studying a representative volume. Despite demonstrating impressive results, these models face a limitation; they cannot comprehensively address both IP and OOP behaviors simultaneously. Consequently, inertial forces due to perpendicular walls are incorrectly taken into account under dynamic loads with these models.

To streamline the examination of the 3D URM structures under dynamic loads, without sacrificing crucial insights into their structural behavior, the rigid macro-element model (RMEM) emerges as a significant advancement [17–19]. This model is adept at simultaneously analyzing IP and OOP behaviors, employing a system of rigid frames linked by both normal and tangential springs. These springs facilitate the simulation of tension/compression and sliding movements within the masonry, while diagonal springs within the frames mimic shear behavior. To support modal and seismic analyses, the RMEM incorporates a mass matrix, enhancing its applicability in dynamic scenarios [20]. However, RMEM encounters challenges in correctly capturing the OOP bending of the wall, which necessitates a fine mesh and, consequently, increases computation time significantly. Moreover, the inclusion of additional structural elements such as frames in the openings can be cumbersome [21]. Yet, a version of the RMEM has been proposed to overcome this issue, albeit leading to a non-negligible increase in the number of degrees-of-freedom (DOF) [22].

In light of the constraints identified in the prevalent models for analyzing 3D URM structures, this paper introduces an enhanced version of the deformable frame model (DFM) proposed by Decret et al. [23]. This model was initially tailored to model URM walls subjected to cyclic IP loads. It is distinguished by its limited number of DOF and the straightforward incorporation of additional structural components such as reinforced concrete or timber frame elements.

The main objectives of this paper are as follows: (i) to introduce an enhanced DFM for the 3D modeling of masonry structures; (ii) to demonstrate that this simplified model, based on planar macro-elements, can effectively capture the 3D elastic dynamic characteristics of masonry structures including mode shapes and natural frequencies; and (iii) to validate the nonlinear constitutive behavior of the macro-elements through transient dynamic analysis.

Section 2 serves as a reminder of the DFM for two-dimensional (2D) modeling. Then, the definition of the DFM for 3D modeling is proposed. In order to model the URM structures submitted to dynamic loading, the DFM mass matrix is defined in Section 3. Finally, in Section 4, modal analysis of two masonry structures and the simulation of a shake table test conducted on a half-scale masonry house are performed using the DFM. These numerical simulations demonstrate the model's suitability for the dynamic analysis of masonry structures.

2. The DFM for IP Load

The DFM, as depicted in Figure 1, operates within the FE method framework, representing a portion of an IP-loaded URM wall, such as, for instance, a masonry infill wall. The approach to modeling masonry structures with the DFM is direct and efficient, eliminating the need to individually identify wall components such as piers and spandrels like in the EFM [4–9] and POR methods [24,25]. This is achieved through a meshing technique that intuitively integrates the presence of openings within the structure. A comparison of the DFM with existing models and an in-depth discussion of the model design and its validation against quasi-static loading scenarios are detailed in [23], of which only the main developments are recalled in this section.

In terms of structure, the DFM is characterized by a minimalistic design, consisting of only four nodes positioned at each corner. Each node is interconnected via three struts (Figure 1). The model's movement is captured through eight DOF, corresponding to two DOF per node, facilitating a comprehensive simulation of the macro-element's response to various types of loads.

The derivation of Equations (1)–(14) is described in detail in [23].

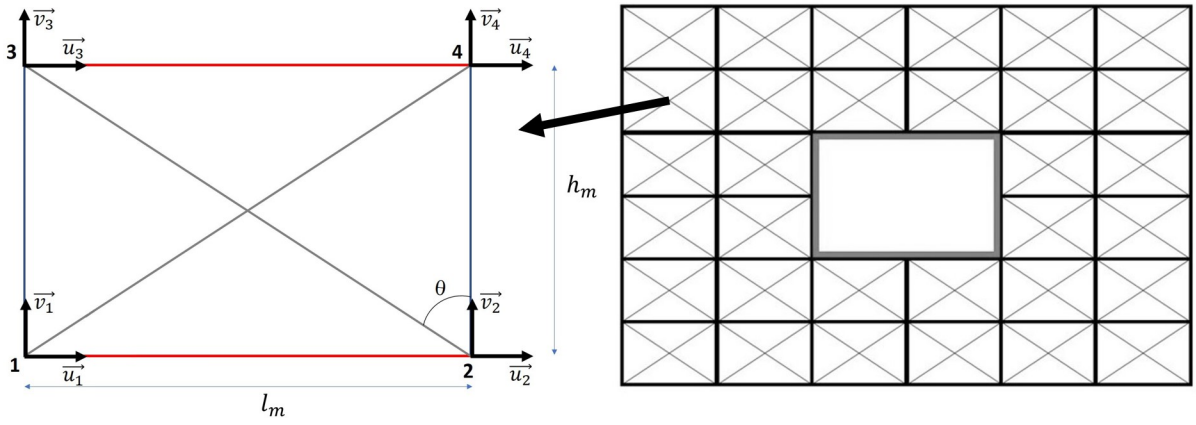

Figure 1. DFM's schematic representation and its integration into the modeling of a wall for IP analysis [23].

2.1. Strut Stiffnesses

The determination of the elastic stiffness for each strut of the DFM incorporates the masonry's Young modulus E_m, the masonry's shear modulus G_m, the macro-element's height h_m, the macro-element's width l_m, and the wall thickness t_m. The definitions of the stiffnesses for the vertical struts K_v, horizontal struts K_h, and diagonal struts K_d are provided by Equations (1)–(3), where θ is the angle, as shown in Figure 1.

$$K_v = E_m \cdot \frac{l_m.t_m}{2.h_m} - K_d.\cos^2(\theta), \tag{1}$$

$$K_h = E_m \cdot \frac{h_m.t_m}{2.l_m} - K_d \cdot \sin^2(\theta), \tag{2}$$

$$K_d = G_m \cdot \frac{l_m.t_m}{2.h_m.\sin^2(\theta)}. \tag{3}$$

2.2. Shear Strength of the Macro-Element

The ultimate force capacity F_u of the diagonal struts is characterized using two distinct equations to accurately reflect two failure mechanisms: the diagonal cracking and shear-sliding of the masonry. For the diagonal cracking failure mode, the formula developed by

Turnšek and Čačovič [26] is used (Equation (4)). For the shear-sliding failure, the Mohr–Coulomb's law, as proposed in [27], is used (Equation (5)).

$$f_{v,1} = \frac{f_t}{b}\sqrt{\frac{\sigma_v}{f_t} + 1}, \tag{4}$$

$$f_{v,2} = \overline{c} + \overline{\mu}\sigma_v. \tag{5}$$

The parameter b in Equation (4) allows accounting for the slenderness of the macro-element (it is reminded that h_m and l_m are the dimensions of the macro element and not of the wall), where b is defined as

$$1 \leqslant b = h_m/l_m \leqslant 1.5. \tag{6}$$

In Equations (4) and (5), σ_v represents the vertical stress exerted on the masonry, and f_t denotes the masonry's tensile strength. For the shear-sliding equation, two additional parameters were included (as introduced by Mann and Müller [27]): the cohesion $\overline{c}$ and the coefficient of friction $\overline{\mu}$. The values for the cohesion and the coefficient of friction were derived using Equations (7) and (8), where H_b and L_b are the height and the width of the bricks, respectively; and c and μ represent the masonry cohesion and friction coefficient, respectively.

$$\overline{c} = \frac{c}{1 + 2 \cdot \mu \cdot \dfrac{H_b}{L_b}}, \tag{7}$$

$$\overline{\mu} = \frac{\mu}{1 + 2 \cdot \mu \cdot \dfrac{H_b}{L_b}}. \tag{8}$$

The ultimate force capacity of the diagonal struts F_u is defined with Equations (4) and (5), taking into account the cross-section of the macro-element and the angle θ, as shown in Equation (9).

$$F_u = \frac{l_m \cdot t_m \cdot \min(f_{v,1}, f_{v,2})}{\sin(\theta)}. \tag{9}$$

2.3. Inelastic Behavior

After considering the different failure modes of the masonry and selecting the associated ultimate forces, as commonly proposed in the literature, a hysteresis model was introduced, as shown in this section, to account for the energy dissipation under cyclic loading, a feature that is particularly important in the case of earthquakes.

The DFM was designed to simulate the behavior of URM structures subjected to shear loading. All of the dissipative phenomena occurring in the masonry are assumed to be reproduced by the diagonal struts. The constitutive force–displacement curve of the diagonal strut is depicted in Figure 2, where the envelope curve is highlighted as a bold black line. This curve is defined by four key parameters: the initial stiffness of the diagonal strut K_d, the force at crack initiation F_{cr}, the maximum strength of the masonry F_u, and the displacement at maximum strength d_u. Of these, K_d and F_u are directly derived from the material and geometric properties of the masonry, as detailed in Equations (3) and (9).

The determination of the remaining parameters is based on the analysis of the cyclic shear tests conducted on masonry piers. In situations where experimental data are unavailable, a simplified approach can be used. This approach represents the constitutive behavior with a bi-linear envelope curve: an initial elastic phase extending up to d_u, followed by a transition to perfectly plastic behavior beyond this point. This simplification helps maintain the analytical tractability of the model while capturing the essential characteristics of the masonry behavior under shear loads.

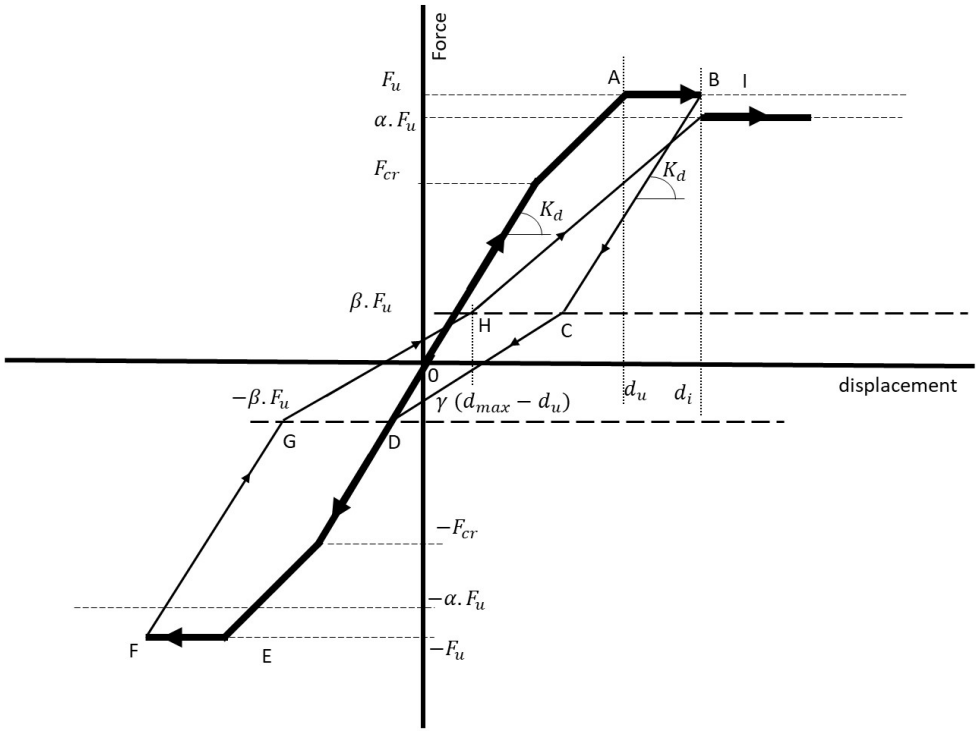

Figure 2. Force/displacement curve of the diagonal strut [23].

The hysteresis model proposed by Panagiotakos and Fardis [28] is used to represent the loading–unloading behavior (Figure 2). This model accounts for stiffness and strength degradation through three parameters: α, β, and γ. These parameters, as well as their dependence on the dimensions of the macro-element, were identified by Decret et al. [23] thanks to simulations of quasi-static cyclic shear tests that were performed on masonry walls. Equations (10)–(12) were used to determine α, β, and γ, respectively.

$$\alpha = 0.9 + \frac{b_{diag} - 1}{1 + \sigma_v / f_t}, \tag{10}$$

$$\beta = 0.2 b_{diag}^2 + (1 - b_{diag})^2, \tag{11}$$

$$\gamma = -0.4 + 2(1 - b_{diag}). \tag{12}$$

The parameter b_{diag} in Equation (10) is analogous to the parameter b used to define the maximum strength of the diagonal element, and it is determined by Equations (13) and (14).

- if $h_{elem} > l_{elem}$,

$$1 \leqslant b_{diag} = h_{elem} / l_{elem} \leqslant 1.5; \tag{13}$$

- if $h_{elem} < l_{elem}$,

$$1 \leqslant b_{diag} = l_{elem} / h_{elem} \leqslant 1.5. \tag{14}$$

3. The DFM for OOP Load

To seamlessly incorporate the OOP behavior of the masonry into the DFM without altering the established nonlinear constitutive behavior of its diagonal struts, the model adopts a strategy in which the strut elements of the frame are transformed into beam elements, as proposed by Quagliarini et al. [12] in the SAM approach. Additional DOF are introduced to capture the OOP bending and torsional behavior of the masonry, while maintaining the IP behavior of the DFM, thereby preserving the role of the diagonal elements.

Figure 3 illustrates the kinematics of the DFM for 3D modeling, highlighting the addition of three new DOF per node. Consequently, the total number of DOF per DFM element increases to 20, comprising 5 DOF.

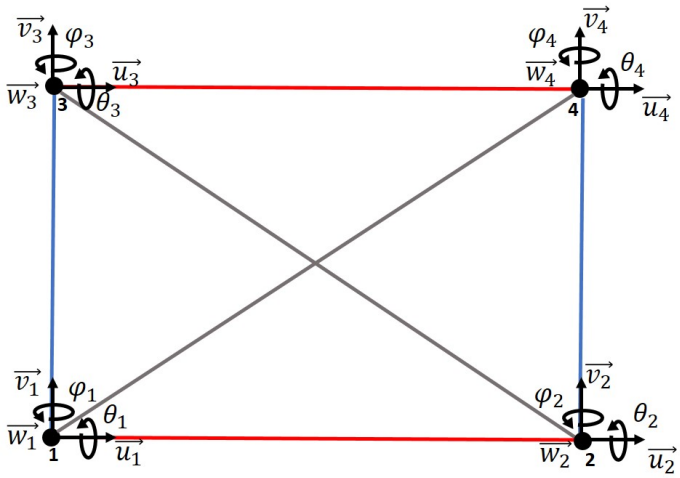

Figure 3. The DFM for 3D modeling with kinematics defined in the global orthonormal coordinate system.

The axial stiffness of the frame's beam elements under axial load was designed to match that of the original struts. Consequently, the axial elastic modulus of the beams E_x does not correspond to the Young's modulus of the masonry E_m. Instead, E_x is a unique modulus of elasticity tailored for axial deformation. It is defined by Equation (15) for vertical beams and by Equation (16) for horizontal beams, where h_{inf} is the height (and l_{inf} is, respectively, the width) of the area of influence of the horizontal beam (the same, respectively, for the vertical beam). They are shown in Figure 4.

$$E_{x,v} = K_v \frac{h_m}{t_m l_{inf}}, \tag{15}$$

$$E_{x,h} = K_h \frac{l_m}{t_m h_{inf}}. \tag{16}$$

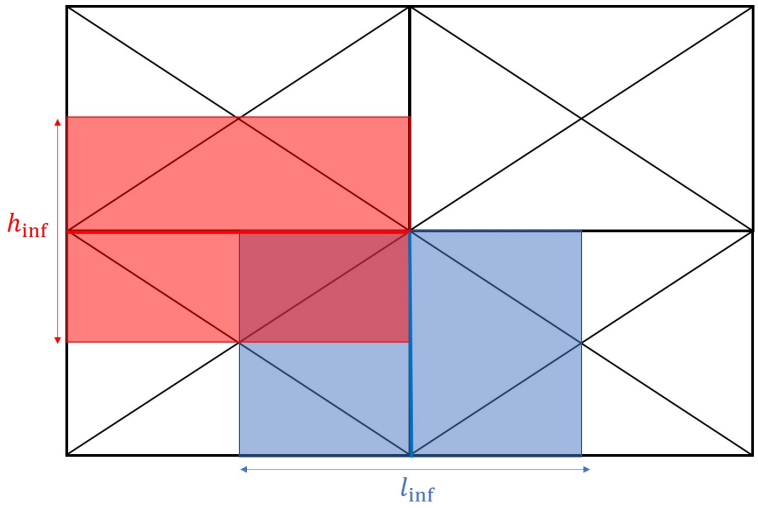

Figure 4. Definition of the height and the width of the influence of the DFM beams.

The diagonal elements provide additional rigidity for vertical and horizontal IP tension/compression loading but offer no rigidity in the OOP direction. Therefore, the bending

behavior of the beams is characterized by the Young's modulus of the masonry E_m rather than the elastic modulus E_x.

A DFM frame beam element of length L is depicted in Figure 5 along with its local coordinate system. This beam is defined with nodes i and j. Let u_i (and, respectively, u_j) denote the axial displacement; v_i (and, respectively, v_j) the vertical displacement; w_i (and, respectively, w_j) the OOP displacement; θ_i (and, respectively, θ_j) the angle related to the bending around the vertical local axis; and φ_i (and, respectively, φ_j) the torsion angle. The displacement vector and the internal force vector of the beam are denoted as

$$\underline{U} = \left\{u_i, v_i, w_i, \varphi_i, \theta_i, u_j, v_j, w_j, \varphi_j, \theta_j\right\}^T, \underline{F} = \left\{N_i, T_{y,i}, T_{z,i}, M_{x,i}, M_{y,i}, N_j, T_{y,j}, T_{z,j}, M_{x,j}, M_{y,j}\right\}^T.$$

The balance Equation (17) defines the relationship between these two vectors through the stiffness matrix $\underline{\underline{K}}$, which is defined by Equation (18).

$$\underline{F} = \underline{\underline{K}}.\underline{U}. \tag{17}$$

$$\underline{\underline{K}} = \begin{bmatrix} \frac{SE_x}{2L} & 0 & 0 & 0 & 0 & -\frac{SE_x}{2L} & 0 & 0 & 0 & 0 \\ & \frac{3E_mI_z}{2L^3} & 0 & 0 & 0 & 0 & -\frac{3E_mI_z}{2L^3} & 0 & 0 & 0 \\ & & \frac{3E_mI_y}{2L^3} & 0 & -\frac{3E_mI_y}{2L^2} & 0 & 0 & -\frac{3E_mI_y}{2L^3} & 0 & -\frac{3E_mI_y}{2L^2} \\ & & & \frac{G_mJ}{2L} & 0 & 0 & 0 & 0 & -\frac{G_mJ}{2L} & 0 \\ & & & & \frac{2E_mI_y}{L} & 0 & 0 & \frac{3E_mI_y}{2L^2} & 0 & \frac{E_mI_y}{L} \\ & & & & & \frac{SE_x}{2L} & 0 & 0 & 0 & 0 \\ & & & & & & \frac{3E_mI_z}{2L^3} & 0 & 0 & 0 \\ & & & & & & & \frac{3E_mI_y}{2L^3} & 0 & \frac{3E_mI_y}{2L^2} \\ & & & \text{sym} & & & & & \frac{G_mJ}{2L} & 0 \\ & & & & & & & & & \frac{2E_mI_y}{L} \end{bmatrix} \tag{18}$$

The inertia terms in Equation (18), i.e., I_z, I_y, and J, are determined with the dimensions of the surrounding macro-elements of the DFM. Their values for the vertical and horizontal beams are provided in Table 1.

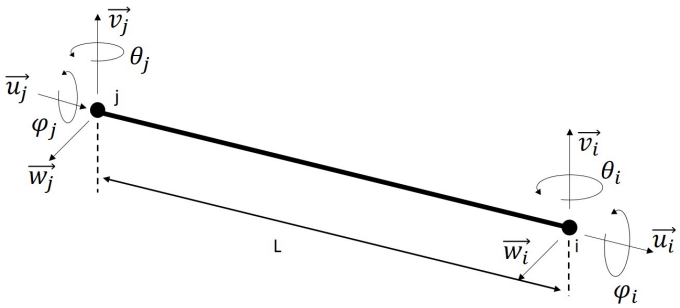

Figure 5. Kinematics of the beam elements of the DFM defined in the local orthonormal coordinate system.

Vertical beams located at junctions where two or more walls intersect at right angles require special consideration. At these corner connections, an IP load on one wall induces an OOP load on the adjoining perpendicular wall. This dual role complicates the accurate specification of the beam properties as their definition can vary depending on the model's mesh size. Standard definitions for beam bending behavior in these cases tend to overestimate the structural stiffness at corners, regardless of mesh density.

Table 1. Definition of the inertia terms of the DFM beam elements.

Inertia Term	Vertical Beam	Horizontal Beam
I_y	$t_m^3.l_{inf}/12$	$t_m^3.h_{inf}/12$
I_z	$t_m.l_{inf}^3/12$	$t_m.h_{inf}^3/12$
J	$I_z + I_y$	$I_z + I_y$

To address this challenge and prevent the overestimation of the corner stiffness, the moments of inertia I_y and I_z for the vertical beams at these critical junctions were intentionally set to zero. This adjustment provides a more realistic representation of the structure's behavior by reducing the stiffness contribution of corner beams, aligning the model's response more closely with the actual structural performance under complex loading conditions.

To accurately represent the structure's torsional behavior, it is essential to maintain a non-zero polar moment of inertia J. Consequently, the standard formula $J = I_z + I_y$ in Table 1 is not adequate for the vertical beams located at the corners of intersecting walls. The intersection of two walls is depicted in Figure 6, where L_1 (and, respectively, L_2) represents the total length of the vertical strut in the x-direction (and, respectively, the y-direction). Additionally, L is the length of influence of the element on the left in Direction 1, and the thickness of the wall oriented in Direction 1 is denoted by T_1 (and, respectively, T_2 in Direction 2). With these notations, the polar moment of inertia of the vertical beam at the corner J_{corner} is defined by Equation (19).

$$J_{corner} = \frac{1}{12}(T_1L_1^3 + L_1T_1^3 + T_2L_2^3 + L_2T_2^3) + L_1T_1((d_x - 0.5L_1)^2 + (d_y - 0.5T_1)^2) + T_2L_2((d_x - (L_1 + 0.5T_2))^2 + (d_y - (T_1 + 0.5L_2)^2). \quad (19)$$

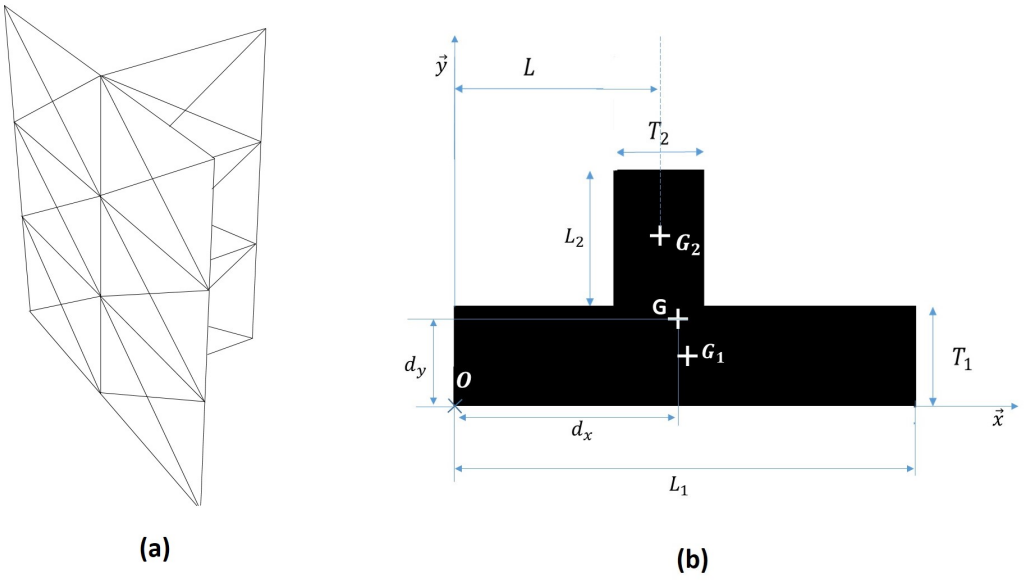

Figure 6. Intersection of two walls: (**a**) intersection modeled with the DFM; (**b**) cross-section of the intersection seen from above.

The distances d_x and d_y represent the coordinates of the center of gravity G of the entire domain of influence of the beam in respect to the reference point O, as shown in Figure 6. These coordinates are defined by Equations (20) and (21).

$$d_x = \frac{(L_1.T_1.L_1/2 + L.L_2.T_2)}{L_1.T_1 + L_2.T_2}, \quad (20)$$

$$d_y = \frac{(L_1.T_1^2 + L_2.T_2.(T_1 + L_2/2))}{L_1.T_1 + L_2.T_2}. \quad (21)$$

It is generally considered that, during an earthquake, the OOP walls slightly contribute to the seismic resistance of the masonry structure. Therefore, the beam elements of the DFM are assumed to exhibit purely elastic behavior. With this assumption, the definition of the DFM for 2D modeling remains unchanged.

4. Mass Matrix of the DFM

The mass matrix of the DFM is defined by lumping the mass at nodal points, considering each node's volume of influence. This volume is calculated as the median distance from each node to the other vertices within the same macro-elements. Two examples of the area of influence are colored yellow and purple in Figure 7a. The yellow area represents a node fully surrounded by DFM elements, resulting in a more typical, often rectangular, area of influence. In contrast, the purple area represents a node located at the periphery of an opening, leading to an irregular, non-rectangular region shaped by the boundaries of the opening.

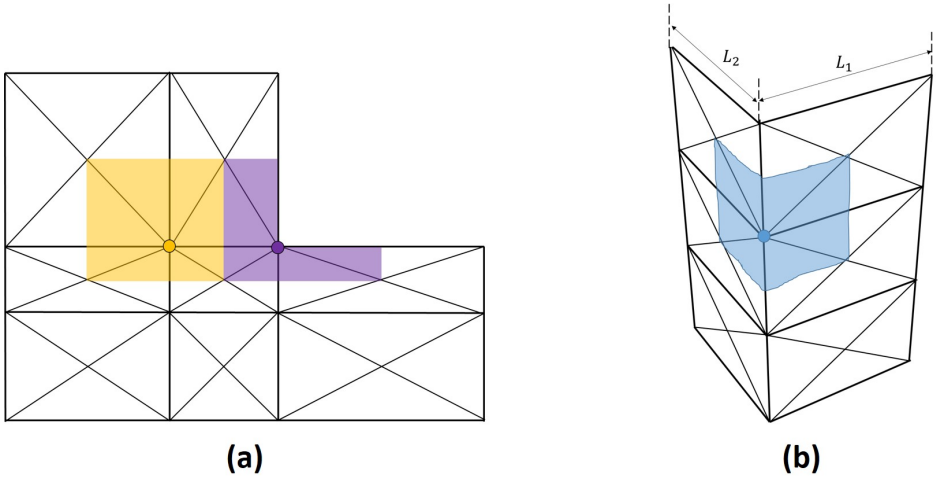

Figure 7. Colored areas show the areas of influence for nodes: (**a**) case when the node is not part of two perpendicular walls; (**b**) case when the node is part of two perpendicular walls.

Equation (22) defines the relationship between the mass M_n at node n, its corresponding area of influence A_n, and the masonry's density ρ_m. This mass is assumed to be identical in all three spacial directions. This approach simplifies the representation of mass distribution by exclusively focusing on the translational mass effects and excluding rotational degrees of freedom from the DFM's mass matrix formulation.

$$M_n = \rho_m A_n t_m. \quad (22)$$

While Equation (22) provides the standard approach for calculating the node mass within the DFM using uniform areas of influence and masonry density, wall intersections introduce unique geometric configurations that require a tailored approach. In typical scenarios, the areas of influence are rectangular, as depicted in Figure 7a. However, at wall intersections, more complex shapes emerge, such as L-shapes, U-shapes, T-shapes, and cross-shapes, as highlighted in Figure 7b by a blue region.

For each of these cases, the mass at the node is not defined by Equation (22) as this would lead to an overestimation. For the example in Figure 7b, the lengths of the area of influence in Direction 1 and 2 are denoted by L_1 and L_2, respectively, and the thickness of the corresponding walls t_1 and t_2, respectively. In this configuration, the area of influ-

ence associated with the node n, represented by a blue circle in Figure 7b, is defined by Equation (23). This equation can be adapted to any intersection of walls.

$$A_{corner} = \begin{cases} (L_1 + 0.5t_2)t_1 + (L_2 + 0.5t_1)t_2 & \text{if } L_1 > t_1 \text{ and } L_2 > t_2 \\ L_1t_1 + L_2L_1 + (L_2 - 0.5t_1)t_2 & \text{if } L_1 < t_1 \text{ and } L_2 > t_2 \\ L_2t_2 + L_2L_1 + (L_1 - 0.5t_2)t_1 & \text{if } L_1 > t_1 \text{ and } L_2 < t_2 \\ L_1L_2 & \text{if } L_1 < t_1 \text{ and } L_2 < t_2 \end{cases}. \quad (23)$$

The mass for the nodes at the intersection of perpendicular walls is defined by Equation (24), where h_{inf} is the height of influence, as defined for the horizontal struts in Figure 4.

$$M_{n,i} = \rho_m A_{corner} h_{inf}. \quad (24)$$

5. Numerical Validation of the Model

To evaluate the DFM's capability in simulating the dynamic behavior of masonry structures, the model was implemented in ATL4S, which is a FE toolbox in MATLAB [29] developed by Grange [30].

The validation process begins with a modal analysis of two different URM structures: a simple square wall and a more complex configuration consisting of five interconnected walls. This initial phase aims to assess the accuracy of the DFM in predicting the natural frequencies and mode shapes of these structures, offering valuable insights into its precision in modeling the dynamic characteristics of URM structures.

Following the modal analysis, the DFM is further tested by simulating a shake table experiment that was conducted by Yadav et al. [31] on a half-scale masonry house. This experiment provides a real-world scenario to test the model's predictive accuracy by comparing the displacements generated by the DFM with those observed in the physical tests. Through this comparison, the model's effectiveness and reliability in capturing the seismic response of masonry structures are thoroughly evaluated, representing a significant advancement in validating the DFM for structural engineering and the analysis of masonry behavior under dynamic loads.

All analyses presented in this paper were conducted on a computer equipped with an Intel® Core™ i5-8250U processor running at 1.6–1.8 GHz and 8.0 GB of RAM (Intel, Santa Clara, CA, USA).

5.1. Modal Analysis

To validate the elastic properties of the DFM and the accuracy of its mass matrix definition, a modal analysis was conducted on two structures assumed to be perfectly embedded in their foundations. The objective of this analysis was to compare the results obtained from a reference 3D numerical analysis with those from the DFM for two simplified, hypothetical structures composed of URM walls. These structures, which lack roofs and reinforcing elements, exhibit deformations that are intentionally simplified and somewhat unrealistic. The selected structures are as follows.

- A square wall: This structure represents a simple yet fundamental form in masonry architecture. It enables the evaluation of the DFM's ability to capture basic vibrational modes and ensures that the model accurately reflects the stiffness and mass distribution of this straightforward structure.
- A five-wall structure with openings: This configuration is designed to test the DFM's effectiveness in simulating the dynamic interactions between adjoining walls, resulting in complex modal behaviors. This structure presents a challenge to the model's ability to handle the increased complexity and interactions that are characteristic of real-world masonry buildings.

The DFM is a simplified model based on macro-elements consisting of beams and struts. For both structures, the primary vibration modes and associated natural frequencies identified by the DFM are compared with results from the numerical software Cast3M [32], which utilizes

a refined mesh of cubic finite elements. This comparison highlights the DFM's effectiveness in capturing the primary vibration modes and assesses the impact of varying mesh sizes within the DFM's computational framework. Note that a convergence study has been performed to make sure the results given by the 3D FE model are relevant as reference [33].

The analysis focuses on the five predominant modes, which are selected based on their associated modal masses, as proposed by Clough et al. [34]. These modes correspond to Modes 1, 5, 10, 23, and 25, which are ordered by increasing natural frequencies. To evaluate the DFM's accuracy in estimating natural frequencies, the error is defined as the absolute relative difference between the natural frequencies predicted by the DFM f_{mod} and those obtained from the FE reference model, f_{ref}. Mathematically, this is expressed as Error=$|(f_{ref} - f_{mod})/f_{ref}|$. This metric provides a clear quantitative assessment of the DFM's precision in determining natural frequencies.

The mechanical properties of the masonry in the modal analysis were derived from the quasi-static tests conducted by Yadav [35]. These properties are detailed in Table 2.

Table 2. Material properties of the masonry.

	Stiffness	
Young's modulus	E_m	44 MPa
Shear modulus	G_m	22.2 MPa
	Shear strength	
Tensile strength	f_t	18.4 kPa
Cohesion	c	27 kPa
Friction coefficient	μ	0.6
	Tri-linear behavior	
Cracks initiation	F_{cr}/F_u	0.5
Displacement at maximal strength	d_u/d_{cr}	6.
	Lintel properties	
Lintel Young modulus	E_l	9 GPa
Lintel Poisson's ratio	ν_l	0.2
Lintel section	A_l	5×5 cm^2
Lintel density	ρ_l	700 kg·m^{-3}

5.1.1. Square Wall

The analyzed square wall had a width of 2.5 m and a thickness of 0.3 m. For this wall, the mesh was designated as $n \times m$, where n represents the number of DFM elements along the wall's width, and m represents the number of DFM elements along its height. For instance, a wall modeled with a single DFM element was labeled as 1×1. Examples of the meshes used for each model are illustrated in Figure 8.

The mode shapes for the primary modes are depicted in Figure 9 for both the DFM and the reference 3D FE model. While minor discrepancies were observed, for instance, in the displacement at the midpoint of the wall for the second OOP bending mode, the overall deformed shapes produced by both models were, fundamentally, identical.

The DFM's estimation of the natural frequencies demonstrated significant accuracy for all but the coarsest 3×3 mesh, which exhibited an error of approximately 12%. The highest error observed with more refined meshes did not exceed 8%, as shown in Figure 10. This figure also highlights how the error varies with mesh refinement: while finer meshes enhance accuracy for certain modes (e.g., Mode 1 and Mode 5), they do not uniformly reduce the error across all modes. Notably, the error for the first vertical tension/compression mode (Mode 4) remains consistently around 8%. This persistent error in Mode 4 suggests an inherent limitation in the DFM's simplified approach to modeling complex structural behaviors. Nonetheless, the achieved accuracy is deemed acceptable for the seismic analysis of masonry buildings.

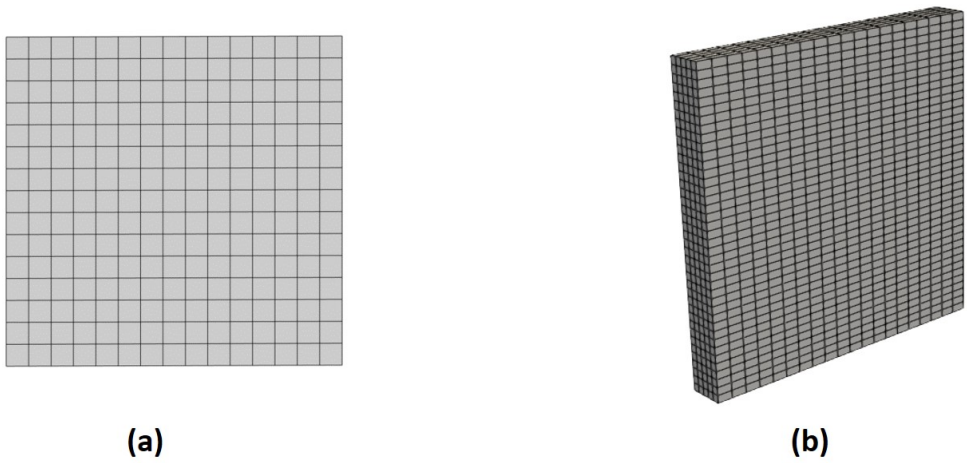

Figure 8. Examples of the mesh used for the square wall: (**a**) 8 × 8 mesh with the DFM ; (**b**) 20 × 30 × 5 mesh with the 3D cubic FE model.

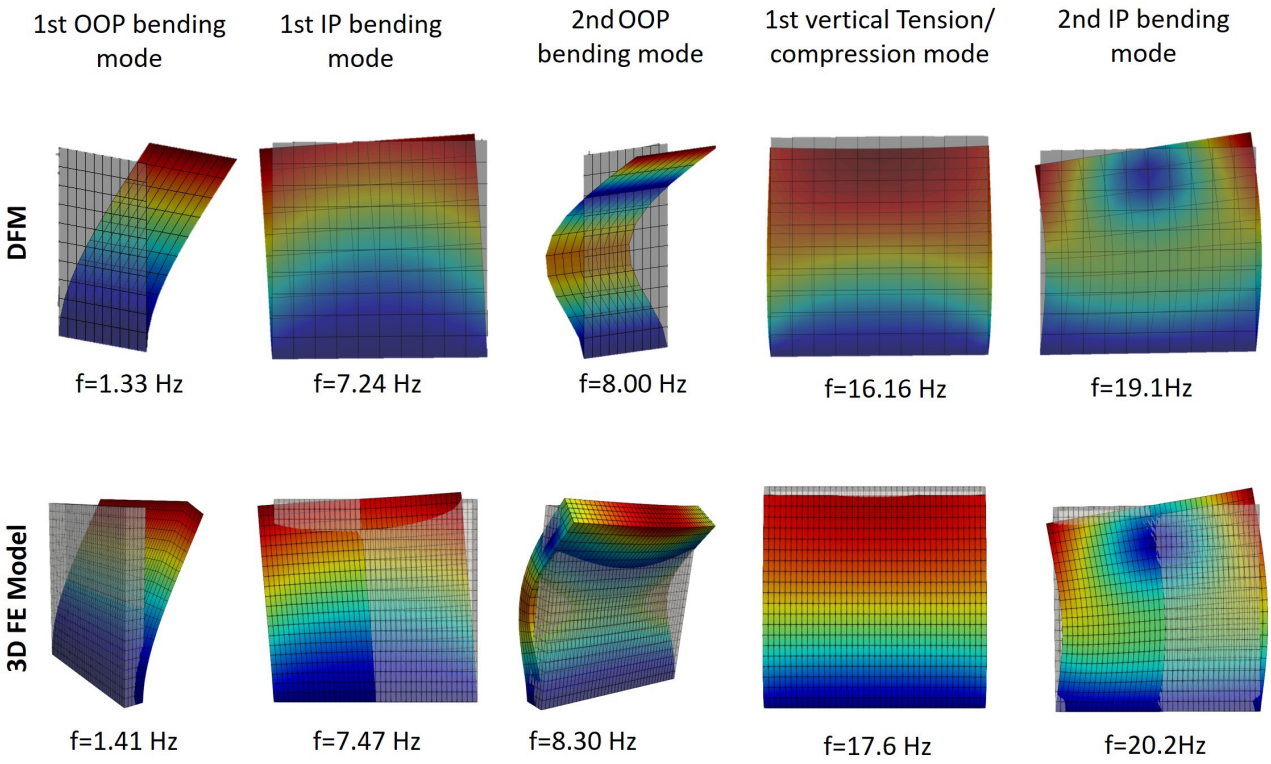

Figure 9. Mode shapes and frequencies for the primary modes computed with the 10 × 10 DFM and the reference 3D FE model.

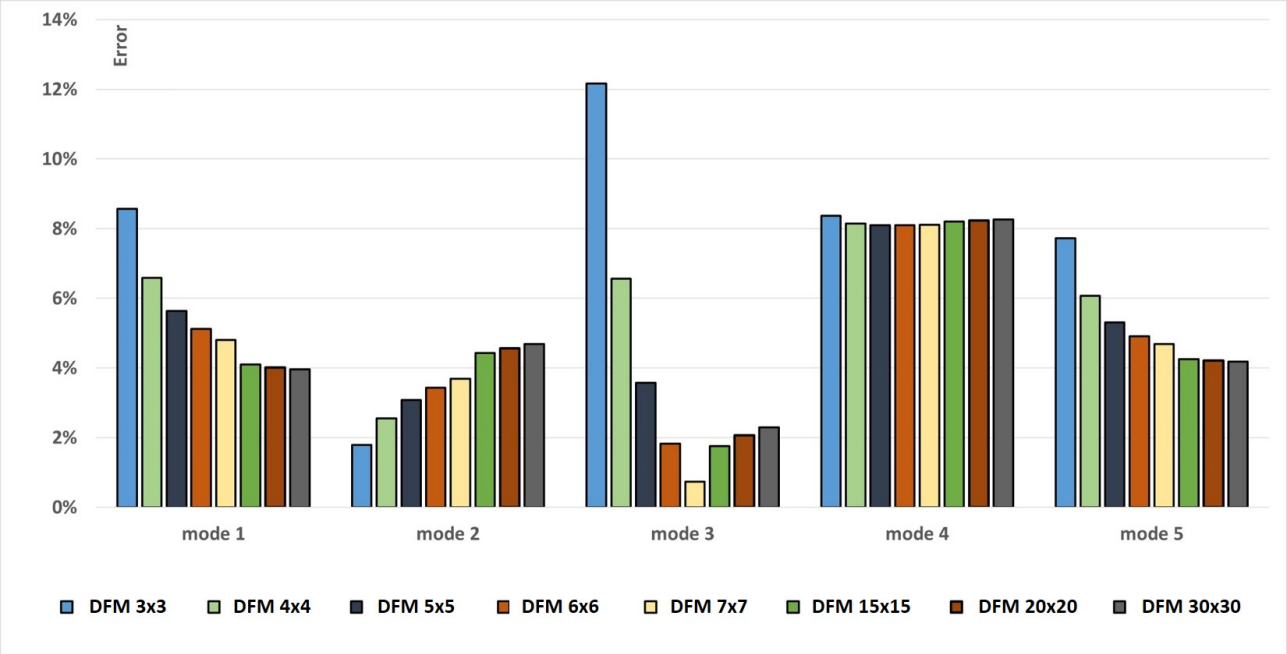

Figure 10. Evolution of error in determining the modes, as depicted in Figure 9, which were analyzed in relation to the mesh size.

The evolution of the natural frequency of the 3rd mode, as depicted in Figure 11, highlights the trend in error determination for this mode and explains why the error did not decrease with finer meshes. Coarser meshes tended to underestimate this frequency, while finer meshes tended to overestimate it. As a result, the 7×7 mesh achieved a more accurate approximation of this frequency compared to even finer meshes.

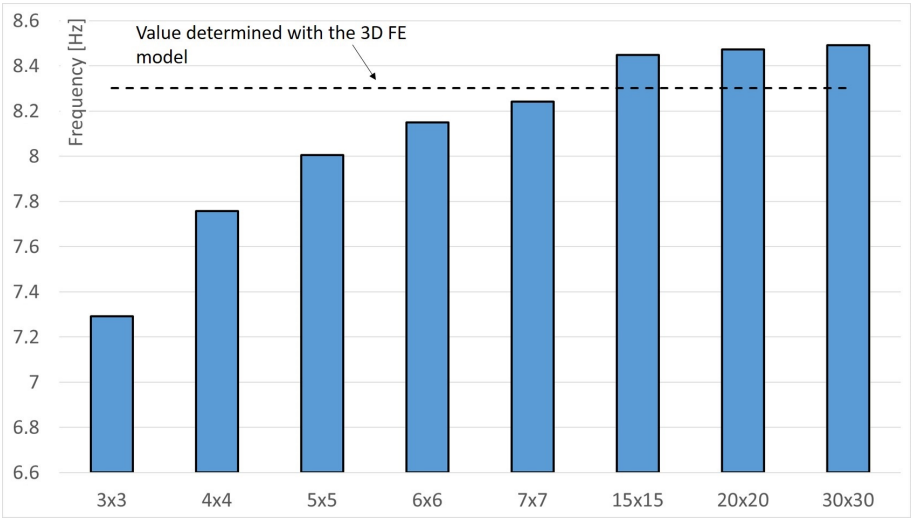

Figure 11. Evolution of the natural frequency value of the 3rd mode analyzed in relation to the mesh size.

This modal analysis of a square wall demonstrated that the DFM accurately captures the primary mode shapes and their corresponding natural frequencies with good precision, even with a limited number of DOF.

5.1.2. Five-Wall Structure with Openings

The layout of the five-wall structure, as illustrated in Figure 12, featured a symmetric design comprising four distinct wall types. One of these, termed the "Window wall", included

a centrally positioned window. Additionally, two walls, labeled "Door wall 1" and "Door wall 2", each featured a centrally positioned door, though with differing dimensions. The fourth wall, which had no opening, shared the same dimensions as "Door wall 2".

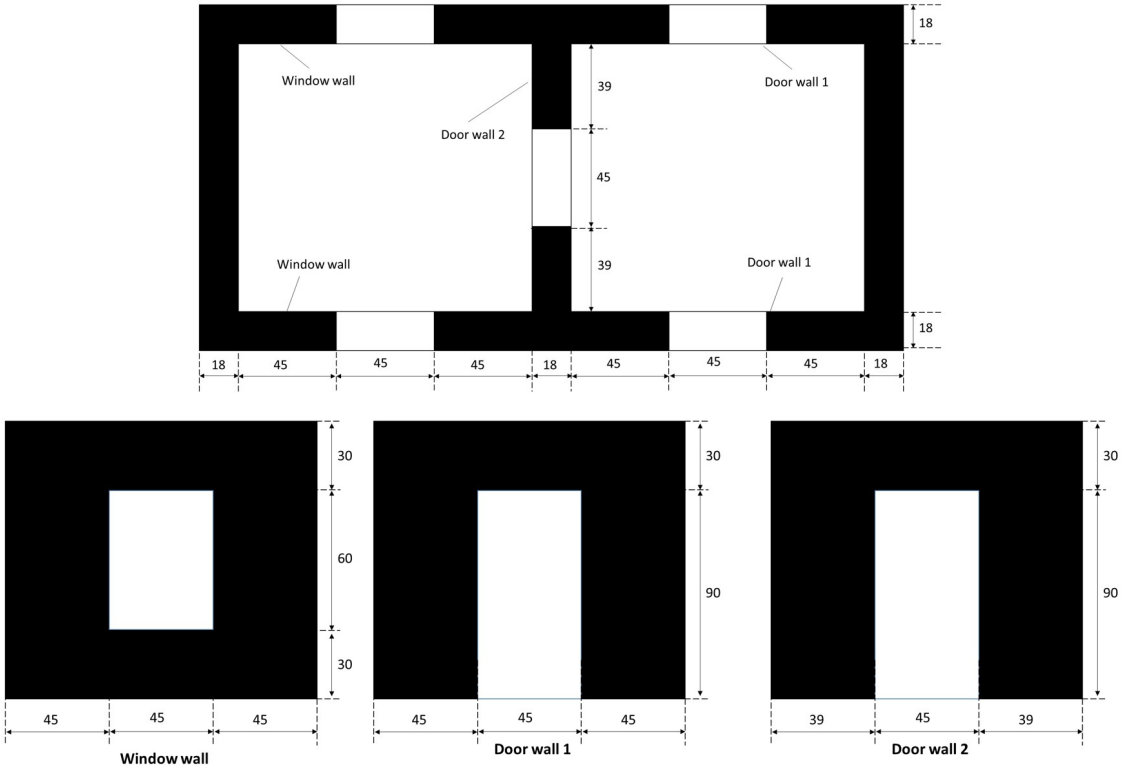

Figure 12. Schemes of the five-wall structure for the modal analysis.

For the five-wall structure, a different naming convention was used for the discretization. All of the meshes consisted of square macro-elements and were identified by a single number n, which represents the level of mesh refinement. $n = 1$ corresponds to the coarsest mesh, where the DFM_1 macro-elements were twice as wide as the DFM_2 macro-elements.

Figure 13 illustrates the modeling of the structure using the DFM (a) and the refined 3D cubic FE model (b).

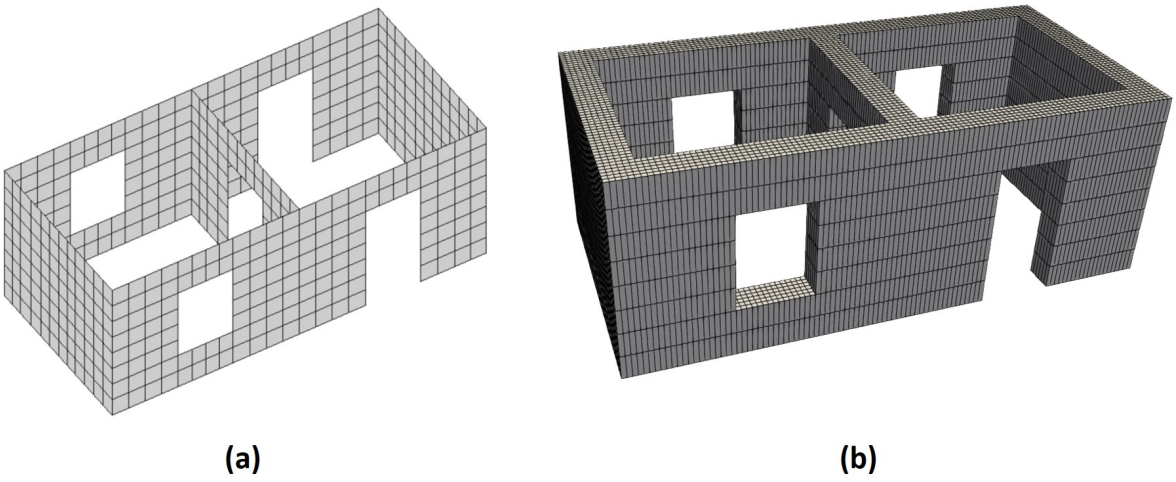

Figure 13. Mesh for the five-wall structure with openings: (**a**) DFM_2; (**b**) 3D FE model.

The comparison of mode shapes derived from the DFM and the 3D cubic FE model, shown in Figure 14, highlights similar dynamic behavior that was predicted by both methods. However, minor differences in the displacement amplitudes were observed, particularly in OOP displacements, mirroring the findings from the square wall analysis.

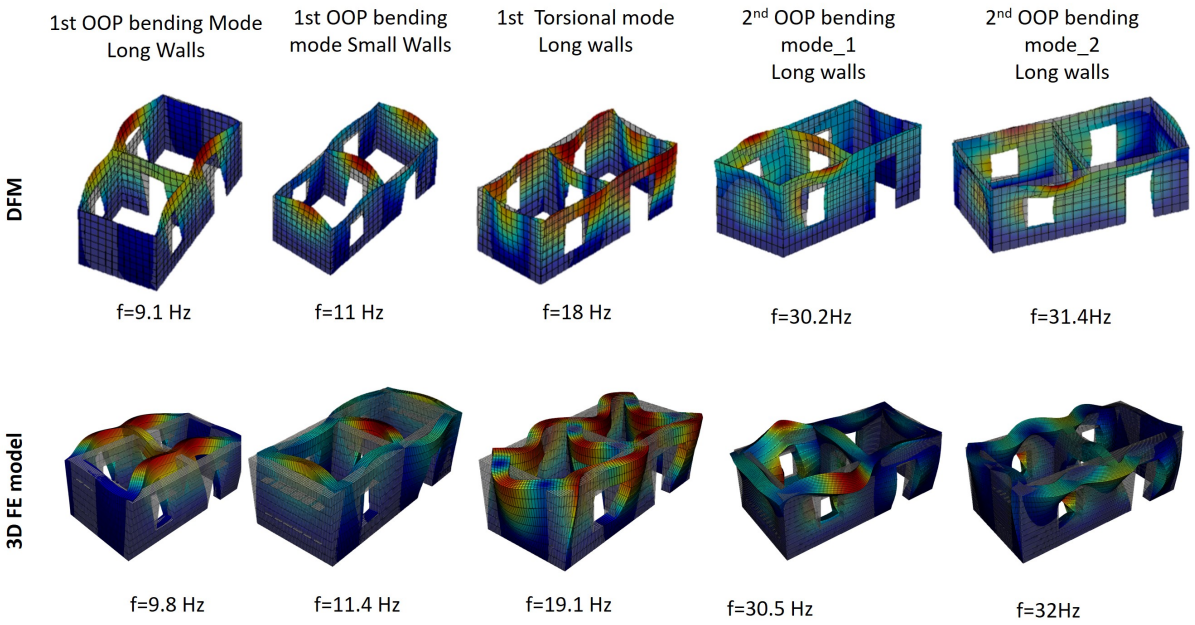

Figure 14. Mode shapes of the five-wall structure with openings.

Figure 15 illustrates the DFM's ability to predict the natural frequencies of the complete structure compared to those obtained from the reference model. The results show that the coarsest mesh provided less accurate predictions, particularly for the first mode, where the error reached 22%. In contrast, the finer meshes considerably improved the accuracy, reducing the maximum error to a more acceptable level of 8%.

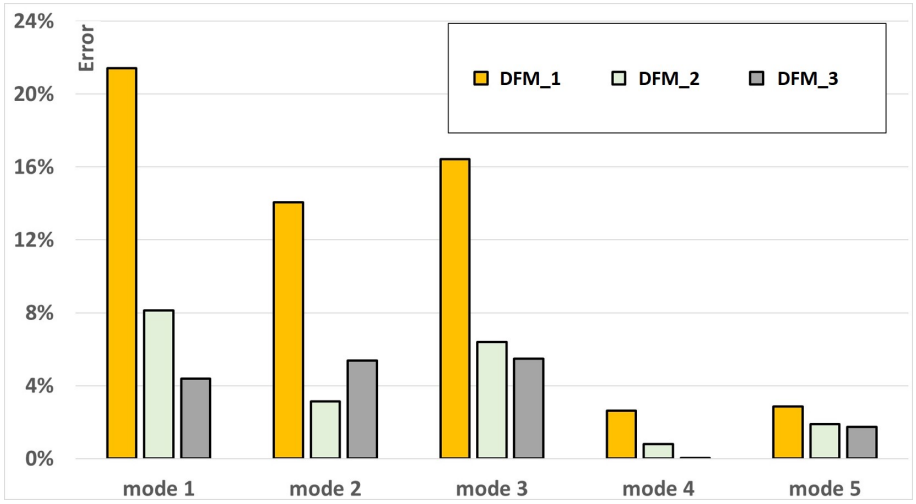

Figure 15. Evolution of the error for the determination of the primary modes with the mesh size.

This analysis confirms that the DFM, especially when applied with an appropriate mesh density, can yield satisfactory results in the modal analysis of complex structures. Despite the inherent simplifications of the DFM, its ability to closely replicate the dynamic behavior predicted by the reference model underscores its effectiveness as a structural analysis tool for evaluating the seismic performance of masonry buildings.

5.2. Dynamic Analysis of a Masonry House

5.2.1. The Studied House

The next phase in validating the DFM for transient dynamic analysis involved the numerical simulation of a dynamic test performed on a structure. The DFM enables 3D transient dynamic analysis of various types of masonry structures. For this validation, the model's performance was evaluated through the simulation of a unidirectional shake table test performed on a half-scale masonry house, as performed by Yadav et al. [31]. It is worth noting that only a few 2D or 3D shake tables exist, and the experimental data from such tests remain limited. Despite the unidirectional nature of the shake table test, 3D effects may arise within the structure. The DFM has demonstrated its ability to capture these effects, such as vertical modes, as confirmed by the modal analysis.

To design the half-scale house model, Cauchy's similitude law was applied, ensuring an accurate scale-down of the prototype's properties to those of the model. This relationship is outlined in Table 3, which illustrates the proportional transformation of the properties of the model (M) relative to the prototype (P). For this shake table experiment, the selected similitude parameters were $\lambda = 0.5$, $e = 1$, and $\rho = 1$.

The model configuration is shown in Figure 16, with specific designations for cardinal orientation: the south wall was positioned on the left side of the figure, while the east and west walls were identified as IP-loaded walls. "Door wall 2" refers to the central partition, and the north wall is at the opposite end. The model had a symmetrical design.

The house was constructed using mud mortar and extruded adobe bricks (175 mm × 125 mm × 50 mm). Its dimensions are shown in Figure 16. The total mass of the masonry structure was about 3.8 tons.

Table 3. Cauchy similitude law.

Quantity	Symbol	Similitude
Length	L	$L_P = \lambda\, L_M$
Modulus of elasticity	e	$E_P = e\, E_M$
Density	ρ	$\rho_P = \rho\, \rho_M$
Area	A	$A_P = \lambda^2 A_M$
Volume	V	$V_P = \lambda^3 V_M$
Mass	m	$m_P = \rho\, \lambda^3\, m_M$
Velocity	v	$v_P = e^{1/2}\, \rho^{-1/2} v_M$
Acceleration	a	$a_P = e\, \lambda^{-1} \rho^{-1}\, a_M$
Force	F	$F_P = e\, \lambda^2 F_M$
Stress	σ	$\sigma_P = e\, \sigma_M$
Time	t	$t_P = e^{-1/2}\, \lambda\, \rho^{1/2}\, t_M$

The results presented in this section pertain to a slightly reinforced masonry house. Figure 17a shows the house during construction, where the only reinforcement consists of timber frames around the doors and windows. In Figure 17b, a speckle pattern can be seen painted on the walls for digital image correlation (DIC) techniques.

Two additional tests were conducted on houses with different seismic strengthening techniques [31]; however, these were not analyzed in the present paper. The focus here was on the structure that exhibited the most significant damage to validate the nonlinear DFM model for masonry walls.

The roof truss was built with timber and covered with galvanized iron (GI) sheeting. It was secured with 10 metal cables—8 along the west and east walls, and 2 along the north and south walls—which passed through the lintel level and were pre-stressed, as seen in Figure 17b. The roof's total mass was approximately 185 kg.

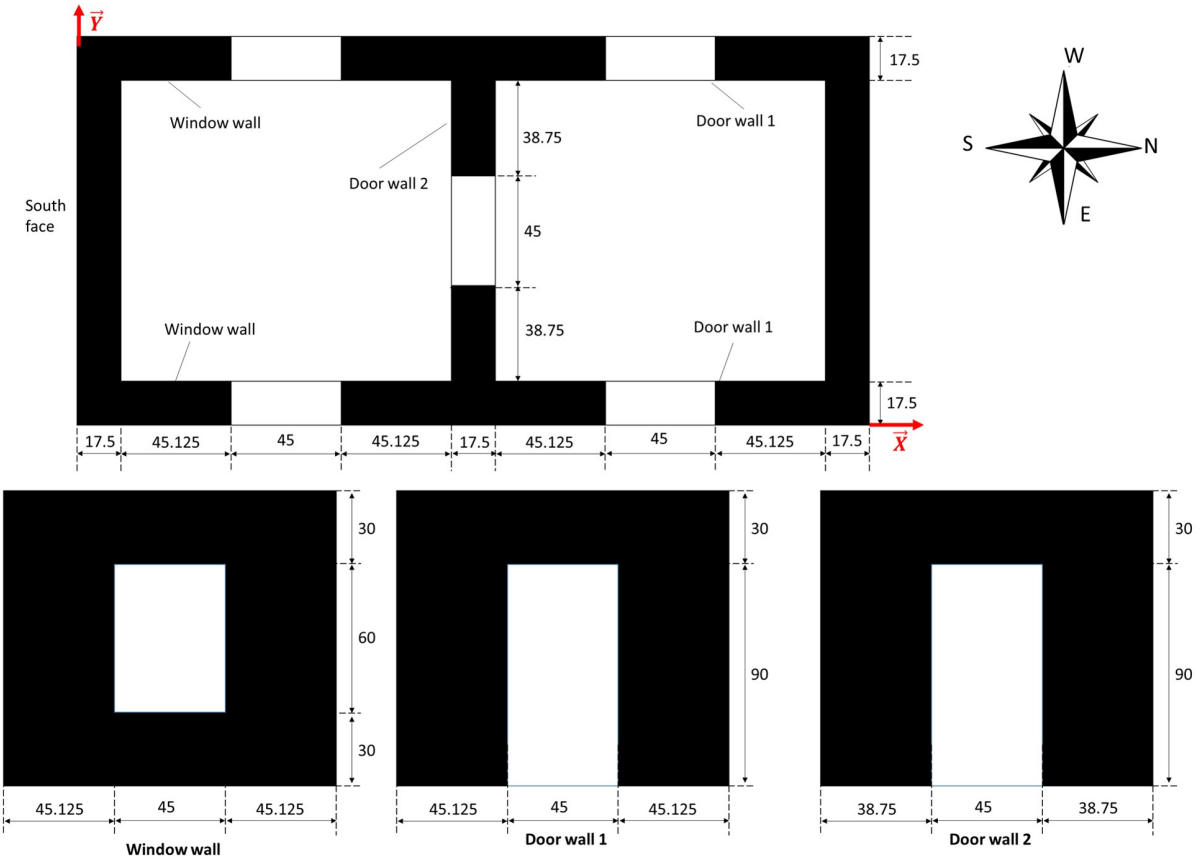

Figure 16. Schemes of the reduced scale house.

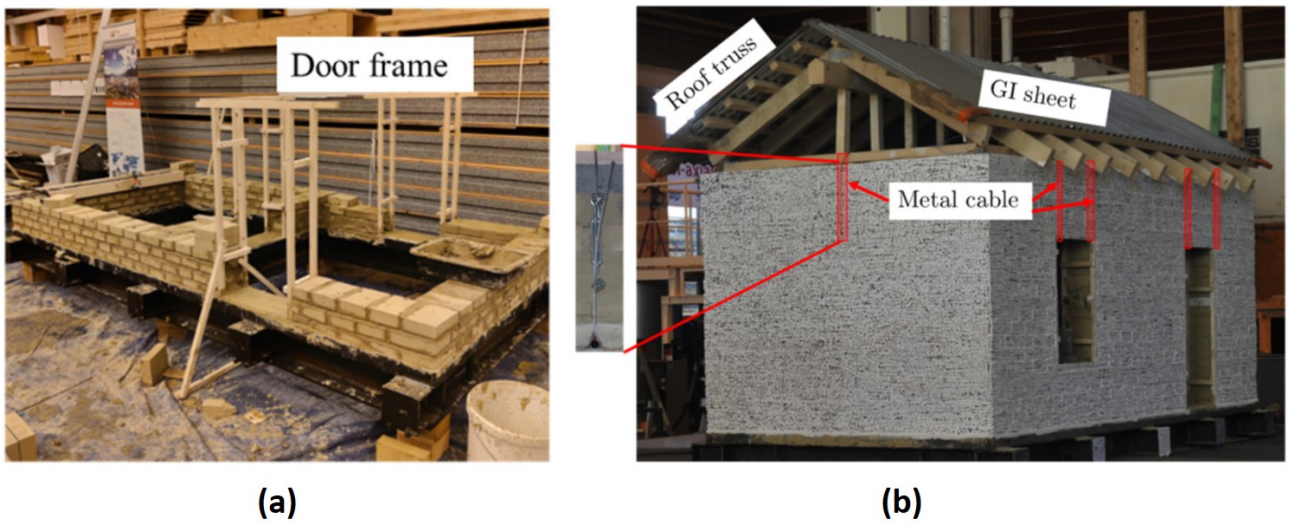

Figure 17. The tested masonry house [31]: (**a**) house construction; (**b**) the roof truss and its connection with masonry house.

5.2.2. Shake Table and Ground Acceleration

The experiment was conducted using the single-axis shake table at the Institut Technologique FCBA in Bordeaux [36]. This shake table is designed to support a maximum dead load of 15 tons. Movement is driven by a servo-hydraulic jack capable of exerting up to 250 kN of force, and it is guided by roller bearings. The shake table's motion is aligned along the X-axis, as illustrated in Figure 16.

The seismic signal used for the experiment is a customized version of the natural acceleration signal recorded during the 2003 Miyagi earthquake in Japan, as measured at the K-Net station. This ground acceleration was modified to reflect the characteristics of a distant subduction earthquake as might be experienced in Guadeloupe, French Caribbean, based on the methodology proposed by Youngs et al. [37]. This methodology modifies the ground acceleration of a known signal in order to obtain a response spectrum featured by the type of soil, earthquake depth, source type, peak ground acceleration, and moment magnitude. For the considered scenario, the peak ground acceleration was 0.35 g.

The adjusted signal corresponded to a reference return period of 475 years on a Type B soil in line with Eurocode 8 standards [10], with a 10% probability of exceeding the reference peak ground acceleration over a span of 50 years. This scenario aligns with the "no collapse" condition specified in Eurocode 8. The response spectrum of the accelerogram and the ground acceleration, as shown in Figure 18, were further scaled using Cauchy's similitude law, yielding a maximum ground acceleration of 0.7 g.

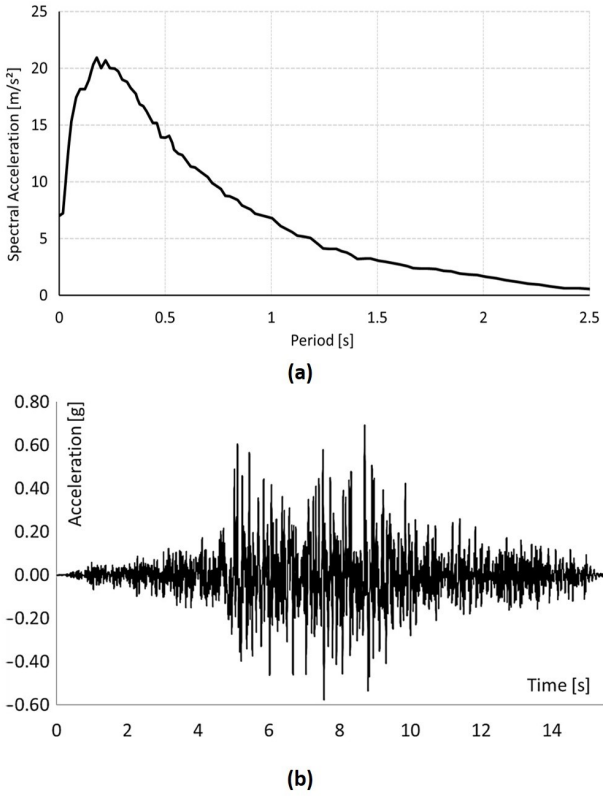

Figure 18. The frequency and time-based data of the seismic signal: (**a**) eesponse spectrum of the accelerogram; (**b**) ground acceleration of the Guadeloupe seismic signal.

5.2.3. Measurements

During the testing phase, displacement data were recorded using cable sensors placed at seven locations along the north wall of the house, as shown in Figure 19. To ensure accuracy and reliability, these measurements were further validated using digital image correlation (DIC) and stereo vision techniques following the methods developed in [38] and [39], as described in [35]. The displacement data from Sensors 6 and 7, located at the top of the east and west walls, served as references for the displacement of the IP-excited walls, while Sensor 2 measured the OOP displacement.

Figure 19. Positions of the cable sensors on the north wall of the reduced scale house.

5.2.4. Numerical Modeling

The representation of the house using the DFM is shown in Figure 20. This mesh corresponds to the DFM_1 mesh used in the modal analysis, consisting of 126 macro-elements and 840 DOF. In this figure, the beam elements and the mass distribution are color-coded for clarity.

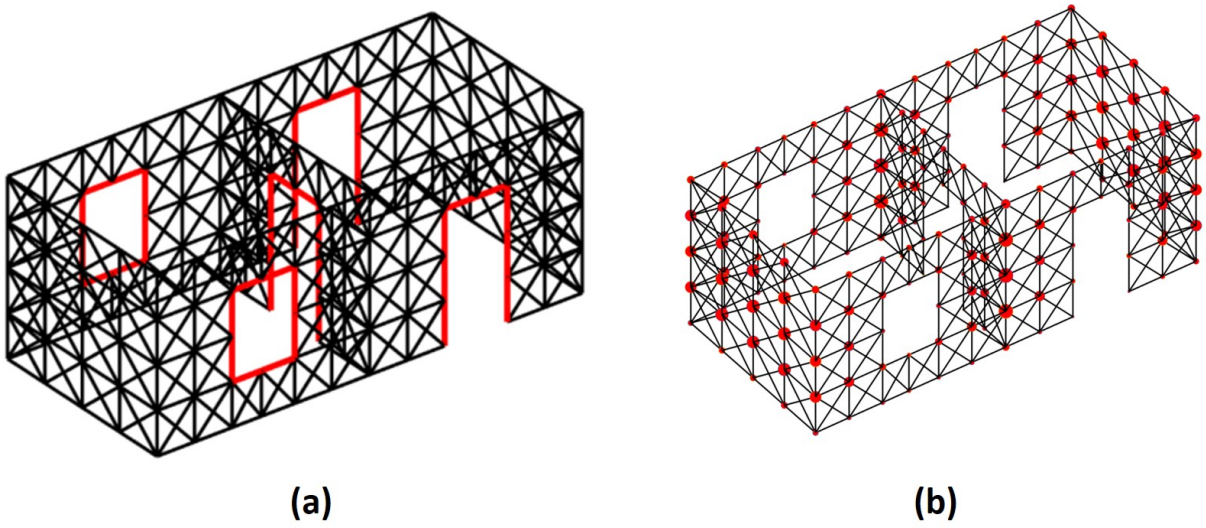

Figure 20. Modeling of the URM house: (**a**) the timber frames around openings, and (**b**) mass distribution.

The roof was treated as a dead load, and it was represented by additional masses at the nodes atop the east and west walls to simulate its weight and impact on structural behavior during an earthquake. The timber frames around the openings were modeled as elastic beams, with their contribution to the overall structural mass calculated using the standard approach for defining the mass matrix of beam elements.

For this study, it was considered that all the dissipative phenomena that occur during an earthquake are modeled thanks to the nonlinear constitutive behavior of the DFM. As a result, there was no additional damping in the dynamic analysis.

The mechanical properties for the numerical analysis are presented in Table 2. These material properties have been identified from the quasi-static tests conducted by Yadav [35] on a wall constructed with the same material.

The five primary modes calculated for the X direction of excitation (Figure 16) correspond to the following frequencies and effective masses (the ratio of modal mass to total

mass): Mode 1 (14.2 Hz, 49.6%); Mode 2 (25.3 Hz, 24.6%); Mode 3 (30.3 Hz, 2.3%); Mode 4 (64.1 Hz, 4%); and Mode 5 (66.3 Hz, 3.1%). Note that Modes 1 and 2 correspond to the OOP displacements of the walls perpendicular to the excitation direction (Figure 21).

The parameters governing the hysteresis behavior are not included in Table 2 as they are derived from the material properties listed in the table and empirical relations outlined in [23]. Their values depend on the location of each macro-element within the structure and are locally determined using Equations (10)–(12). No DFM material properties were calibrated using the shake table test results, ensuring that the DFM serves as a fully predictive model.

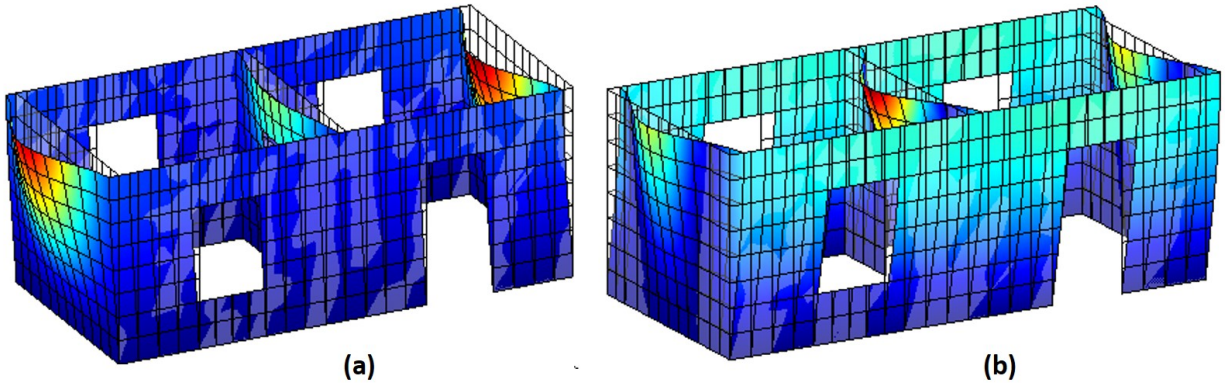

Figure 21. (**a**) Mode 1: 14.2 Hz, effective mass = 49.6%; and (**b**) Mode 2: 25.3 Hz, effective mass = 24.6%.

The displacement corresponding to the ground acceleration shown in Figure 18 was applied to the shake table on which the house model was mounted.

Figure 22 displays the average of the measured displacements at Points 6 and 7 alongside the displacement calculated at Point 6 using the DFM (the calculated displacements at Points 6 and 7 are identical due to symmetry). Focusing on the time interval between 4 s and 12 s, when displacements reach their peak values, they provide insights into the numerical model's performance relative to the actual behavior of the tested house.

Despite the overall accuracy, noticeable deviations exist between the model predictions and the experimental observations, particularly around the 7 s mark, where the model fails to accurately capture the measured oscillations. The most significant discrepancy occurs at the peak displacement at 9 s, where the model underestimates the experimentally recorded displacement. This limitation can be attributed to the model's inability to accurately reproduce the OOP displacement, as shown in Table 4, where the OOP displacement value is only half of the experimentally measured value.

Furthermore, Table 4 presents the maximum displacements captured by the DFM alongside those experimentally recorded during the shake table test at Points 6 and 7 (d_{IP}) and at Point 2 (d_{OOP}). These results highlight the model's performance in replicating the IP wall movements in both negative and positive directions, achieving a maximum error of around 10%. However, the model's accuracy declined for displacements in the positive direction, with errors reaching up to 27% at the peak displacement around the 9-second mark. It is important to emphasize that this peak error does not reflect the overall trend throughout the testing period. While the model is generally reliable, certain dynamic responses may occasionally result in deviations from the measured values.

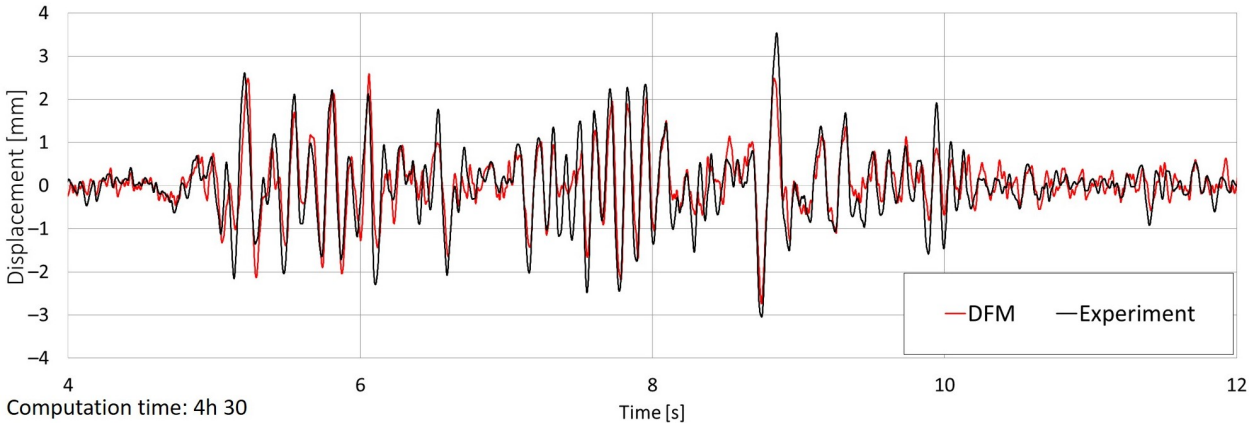

Figure 22. The experimental and calculated displacement histories of the house at Points 6 and 7.

Table 4. Comparison of the maximum displacements in the positive and negative directions determined with the DFM and experimentally measured.

$d_{IP,DFM}$ mm	$d_{IP,exp}$ mm	$error_{IP}$ %	$d_{OOP,DFM}$ mm	$d_{OOP,exp}$ mm	$error_{OOP}$ %
+2.59	+3.54	26.9	+3.74	+7.77	51.9
−2.74	−3.04	10	−3.46	−7.31	52.7

The model's underestimation of the OOP displacement can be attributed to the simplifications inherent in modeling OOP behavior using an elastic constitutive model. Masonry, particularly adobe, exhibits nonlinear behavior when subjected to OOP forces, which can result in cracking, crushing, or other failure modes that a a purely elastic model cannot fully capture. Yadav et al. [31] presented the shake table test results. Unlike the IP walls, the OOP walls exhibited no significant damage under the analyzed seismic excitation level, and the displacements measured at Points 2–5 (Figure 19) linearly varied along the height of the wall. These observations support the model's assumption of linear elastic behavior for OOP walls as a reasonable approximation. Consequently, the authors believe that the underestimation of OOP displacements has minimal impact on the structural response of the IP shear walls, which are the primary contributors to the structure's seismic resistance.

Note that a finer mesh (corresponding to DFM_2) leads to a slightly better accuracy, as shown in Table 5. However, this accuracy sacrifices the computational time (which is about four times longer) for a low impact on the IP behavior.

Table 5. Finer mesh: comparison of the maximum displacements in the positive and negative directions determined with the DFM and experimentally measured.

$d_{IP,DFM}$ mm	$d_{IP,exp}$ mm	$error_{IP}$ %	$d_{OOP,DFM}$ mm	$d_{OOP,exp}$ mm	$error_{OOP}$ %
+2.72	+3.54	23	+4.90	+7.77	37
−2.77	−3.04	9	−3.84	−7.31	48

The computation time of 4 h and 30 min, as indicated in Figure 22, encompasses various tasks, including mesh generation, the calculation of the vertical stress applied to each macro-element, application of static loads, and the execution of the numerical analysis. This overall computation time was considered quite satisfactory as it allows for a comprehensive evaluation of the seismic response of an entire masonry structure within just a few hours.

6. Conclusions

This paper introduced additional features to the DFM, which is a macro-model designed for any type of masonry walls. The DFM offers a practical and computationally efficient alternative to complex finite element approaches for analyzing and understanding the 3D behavior of masonry structures under dynamic loads, such as seismic events. By incorporating specialized beam kinematics within the DFM framework, the model effectively represents the OOP behavior of walls. Walls subjected to IP loads primarily contribute to the seismic resistance, and the model's damage prediction for these shear walls facilitates the evaluation of the seismic vulnerability of masonry structures. Assuming linear elastic behavior for OOP walls, the model achieves a balance between analytical simplicity and the accurate representation of essential response characteristics.

Furthermore, the 2D modeling approach with diagonal struts introduced by Decret et al. [23] was extended to the new 3D model, ensuring that the constitutive relations identified for IP loading remain applicable for 3D analysis. The introduction of a 20-DOF framework for 3D modeling, along with a mass matrix that concentrates mass at the vertices of the DFM, represents a significant advancement in efficiently modeling complete masonry structures under seismic excitation while reducing computational demand.

The validation of this approach through modal analysis, via comparing the DFM's output against that of a conventional 3D cubic FE model, indicated that, despite the coarse mesh used in the DFM, it provides a commendable approximation of mode shapes and natural frequencies. The DFM's validation also extended to the simulation of a shake table experiment that was performed on a half-scale house, as conducted by Yadav et al. [31].

These validations underscore the DFM's utility as a valuable tool in the seismic assessment of masonry structures, balancing computational efficiency with reasonable accuracy in predicting dynamic responses. However, limitations were observed in accurately estimating the OOP displacements, primarily due to the assumption of elastic behavior in this direction. Despite this, the model represents a significant advancement in the dynamic analysis of masonry structures, suggesting areas for future improvement and refinement, particularly in enhancing the modeling of OOP responses to more accurately reflect the complexities observed during seismic events.

Efforts have been made to design the DFM to be as user friendly as possible. Now that it is configured for 3D analysis, the objective is to implement it in widely used software such as POR2000 [25] or SAP 2000 [40]. This aims to make the model accessible to engineers worldwide, enabling them to assess seismic fragility and resilience [41] or to simulate local masonry constructions similar to the projects involving masonry structures with horizontal inclusions in Nepal, as was conducted by Yadav et al. [31] and Decret [33].

Author Contributions: Methodology, D.D. and L.D.; Software, D.D.; Validation, D.D.; Investigation, D.D.; Writing—original draft, D.D.; Writing—review & editing, L.D.; Supervision, Y.M., Y.S., F.V.-C., and L.D.; Funding acquisition, L.D. All authors have read and agreed to the published version of the manuscript.

Funding: This research received no external funding.

Data Availability Statement: Data is contained within the article.

Acknowledgments: This research received support from Univ. Grenoble Alpes to fund the PhD grant of the first author.

Conflicts of Interest: The authors declare no conflicts of interest.

Nomenclature

List of abbreviations

2D	Two-dimensional
3D	Three-dimensional
DFM	Deformable frame model
DIC	Digital image correlation
DOF	Degrees of freedom
EFM	Equivalent frame model
FE	Finite element
FEMA	Federal emergency management agency
GI	Galvanized iron
IP	In-plane
OOP	Out-of-plane
RBSM	Rigid body spring model
REM	Rigid element model
RMEM	Rigid macro-element model
SAM	Simplified analysis of masonry
URM	Unreinforced masonry

List of symbols

A_n	Area of influence at node n
b	Parameter accounting for the element slenderness
c	Masonry cohesion
$\overline{c}$	Masonry cohesion (as proposed by Mann and Muller)
d_{max}	Maximum displacement reached in the opposite direction by the DFM Diagonal strut
d_u	Displacement at the ultimate strength of the DFM diagonal strut
E_l	Lintel Young modulus
E_m	Masonry Young modulus
$E_{x,h}$	Axial stiffness of the DFM horizontal beams
$E_{x,v}$	Axial stiffness of the DFM vertical beams
f_t	Masonry tensile strength
F_{cr}	Force at crack initiation of the DFM diagonal strut
F_u	Ultimate strength of the DFM diagonal strut
$f_{v,1}$	Masonry shear strength for the diagonal cracking failure
$f_{v,2}$	Masonry shear strength for shear-sliding failure
G_m	Masonry shear modulus
H_b	Brick height
h_{inf}	Height of the area of influence of a horizontal strut
h_m	Macro-element height
K_d	DFM diagonal strut initial stiffness
$K_{d,i}$	Initial stiffness of the diagonal strut *i*
K_h	DFM horizontal strut in-plane stiffness
K_v	DFM vertical strut in-plane stiffness
L_b	Brick length
l_{inf}	Width of the area of influence of a vertical strut
l_m	Macro-element width
M_n	Nodal mass at node n
t_m	Macro-element thickness
α	Parameter accounting for the cyclic damage in the masonry
β	Parameter accounting for the cyclic shear behavior of masonry
γ	Parameter accounting for plasticity in the hysteretic behavior
μ	Masonry friction coefficient
$\overline{\mu}$	Masonry friction coefficient as proposed by Mann and Muller
ν_l	Lintel Poisson's ratio
ρ_m	Masonry density
ρ_l	Lintel density

σ_v	Vertical stress applied on the macro-element
θ	Angle of the macro-element diagonal strut with the vertical axis
$u_i, v_i, w_i, \varphi_i, \theta_i$	DOF at node i
$N_i, T_{y,i}, T_{z,i}, M_{x,i}, M_{y,i}$	Forces at node i
$\underline{\underline{K}}$	Stiffness matrix of DFM beam elements
I_y, I_z,J	Inertia terms of DFM beam elements

References

1. Valente, M. Seismic behavior and damage assessment of two historical fortified masonry palaces with corner towers. *Eng. Fail. Anal.* **2022**, *134*, 106003. [CrossRef]
2. Valente, M. Earthquake response and damage patterns assessment of two historical masonry churches with bell tower. *Eng. Fail. Anal.* **2023**, *151*, 107418. [CrossRef]
3. *ABAQUS®*, Theory Manual, Version 6.14; ABAQUS, Inc.: Providence, RI, USA, 2014.
4. Lagomarsino, S.; Penna, A.; Galasco, A.; Cattari, S. TREMURI program: An equivalent frame model for the nonlinear seismic analysis of masonry buildings. *Eng. Struct.* **2013**, *56*, 1787–1799. [CrossRef]
5. Magenes, G.; Della Fontana, A. Simplified non-linear seismic analysis of masonry buildings. *Proc. Br. Mason. Soc.* **1998**, *8*, 190–195.
6. Tomazevic, M.; Weiss, P. A rational, experimentally based method for the verification of earthquake resistance of masonry buildings. In Proceedings of the Fourth US National Conference on Earthquake Engineering, Palm Springs, CA, USA, 20–24 May 1990; Volume 2, pp. 349–359.
7. Pasticier, L.; Amadio, C.; Fragiacomo, M. Non-linear seismic analysis and vulnerability evaluation of a masonry building by means of the SAP2000 V. 10 code. *Earthq. Eng. Struct. Dyn.* **2008**, *37*, 467–485. [CrossRef]
8. Gambarotta, L.; Lagomarsino, S. Sulla risposta dinamica di pareti in muratura. In Proceedings of the Atti del Convegno Nazionale "La Meccanica delle Murature tra Teoria e Progetto", Pitagora editrice, Messina, Italy, 18–20 September 1996; pp. 18–20.
9. Esmaeiltabar, P.; Vaseghi, J.; Khosravi, H. Nonlinear macro modeling of slender reinforced concrete shear walls. *Struct. Concr.* **2019**, *20*, 899–910. [CrossRef]
10. CEN. *Eurocode 8: Design of Structures for Earthquake Resistance-Part 1: General Rules, Seismic Actions and Rules for Buildings*; European Committee for Standardization: Brussels, Belgium, 2005.
11. FEMA. *FEMA 356: Prestandard and Commentary for the Seismic Rehabilitation of Buildings*; Federal Emergency Management Agency: Washington DC, USA, 2000.
12. Quagliarini, E.; Maracchini, G.; Clementi, F. Uses and limits of the Equivalent Frame Model on existing unreinforced masonry buildings for assessing their seismic risk: A review. *J. Build. Eng.* **2017**, *10*, 166–182. [CrossRef]
13. Casolo, S.; Pena, F. Rigid element model for in-plane dynamics of masonry walls considering hysteretic behaviour and damage. *Earthq. Eng. Struct. Dyn.* **2007**, *36*, 1029–1048. [CrossRef]
14. Casolo, S. Modelling in-plane micro-structure of masonry walls by rigid elements. *Int. J. Solids Struct.* **2004**, *41*, 3625–3641. [CrossRef]
15. Casolo, S.; Pena, F. Modelling micro-structure aspects of masonry walls by a simplified approach. *WIT Trans. Built Environ.* **2003**, *66*.
16. Casolo, S. Macroscale modelling of microstructure damage evolution by a rigid body and spring model. *J. Mech. Mater. Struct.* **2009**, *4*, 551–570. [CrossRef]
17. Caliò, I.; Marletta, M.; Pantò, B. A simplified model for the evaluation of the seismic behaviour of masonry buildings. In Proceedings of the 10th International Conference on Civil, Structural and Environmental Engineering Computing, Rome, Italy, 30 August–2 September 2005; Civil-Comp Press: Stirlingshire, UK, 2005; Volume 195.
18. Pantò, B.; Caliò, I.; Lourenço, P.B. A 3D discrete macro-element for modelling the out-of-plane behaviour of infilled frame structures. *Eng. Struct.* **2018**, *175*, 371–385. [CrossRef]
19. Chácara, C.; Cannizzaro, F.; Pantò, B.; Caliò, I.; Lourenço, P.B. Assessment of the dynamic response of unreinforced masonry structures using a macroelement modeling approach. *Earthq. Eng. Struct. Dyn.* **2018**, *47*, 2426–2446. [CrossRef]
20. Chácara, C.; Lourenço, P.B.; Pantò, B.; Cannizzaro, F.; Caliò, I. Macro-element mass matrix for the dynamic assessment of unreinforced masonry structures. In Proceedings of the Congreso de Métodos Numéricos en Ingeniería, Valencia, Spain, 3–5 July 2017.
21. Pantò, B.; Silva, L.; Vasconcelos, G.; Lourenço, P. Macro-modelling approach for assessment of out-of-plane behavior of brick masonry infill walls. *Eng. Struct.* **2019**, *181*, 529–549. [CrossRef]
22. Pantò, B.; Rossi, P.P. A new macromodel for the assessment of the seismic response of infilled RC frames. *Earthq. Eng. Struct. Dyn.* **2019**, *48*, 792–817. [CrossRef]
23. Decret, D.; Malecot, Y.; Sieffiert, Y.; Vieux-Champagne, F.; Daudeville, L. A new macro-element for the prediction of masonry structures behavior. *Buildings* **2024**, *14*, 768. [CrossRef]
24. Tomazevic, M. *The Computer Program POR, Report ZRMK*; Institute for Testing and Research in Materials and Structures: Ljubljiana, Slovenia, 2016.
25. POR2000. Structural and Seismic Calculation and Analysis of Masonry Structures. Newsoft. Available online: https://www.newsoft-eng.it/software/por-2000 (accessed on 24 October 2024).

26. Turnšek, V.; Čačovič, F. Some experimental results on the strength of brick masonry walls. In Proceedings of the 2nd International Brick Masonry Conference, Stoke-on-Trent, UK, 12–15 April 1970; pp. 149–156.
27. Mann, W.; Müller, H. Failure of shear-stressed masonry: An enlarged theory, tests and application to shear walls. *Proc. Br. Ceram. Soc.* **1982**, *30*, 223–235.
28. Panagiotakos, T.; Fardis, M. Seismic response of infilled RC frames structures. In Proceedings of the 11th world conference on earthquake engineering, Acapulco, Mexico, 23–28 June 1996; Volume 23, p. 28.
29. Mathworks. *Matlab Version: 9.4 (R2022b)*; The MathWorks Inc.: Natick, MA, USA, 2022.
30. Grange, S. *ATL4S, a Tool and Language for Simplified Structural Solution Strategy*; Technical report; GEOMAS Insa-Lyon: Lyon, France 2016.
31. Yadav, S.; Sieffert, Y.; Vieux-Champagne, F.; Malecot, Y.; Hajmirbaba, M.; Arléo, L.; Crété, E.; Garnier, P. Shake table tests on 1:2 reduced scale masonry house with the application of horizontal seismic bands. *Eng. Struct.* **2023**, *283*, 115897. [CrossRef]
32. Cast3M version 24.1. Finite Element Tool Box for Structural and Fluid Mechanics. Available online: https://www-cast3m.cea.fr (accessed on 24 October 2024).
33. Decret, D. Numerical Model for the Assessment of the Seismic Vulnerability of Traditional Masonry Structures with Seismic Bands. Ph.D. Thesis, Université Grenoble Alpes, Grenoble, France, 2021.
34. Clough, R.W.; Penzien, J. *Dynamics of Structures*, 2nd ed.; McGraw-Hill: New York, NY, USA, 1993.
35. Yadav, S. Horizontal Seismic Band in Masonry Structure: Seismic Vulnerability Analysis Using Experiments. Ph.D. Thesis, Université Grenoble Alpes, Grenoble, France, 2021.
36. FCBA. Seismic Testing of Nepalese Bio-Sourced Buildings. 2020. Available online: https://www.fcba.fr/essais-sismiques-constructions-biosourcees-nepalaises/ (accessed on 10 March 2024).
37. Youngs, R.; Chiou, S.J.; Silva, W.; Humphrey, J. Strong ground motion attenuation relationships for subduction zone earthquakes. *Seismol. Res. Lett.* **1997**, *68*, 58–73. [CrossRef]
38. Sieffert, Y.; Vieux-Champagne, F.; Grange, S.; Garnier, P.; Duccini, J.C.; Daudeville, L. Full-field measurement with a digital image correlation analysis of a shake table test on a timber-framed structure filled with stones and earth. *Eng. Struct.* **2016**, *123*, 451–472. [CrossRef]
39. Vieux-Champagne, F.; Sieffert, Y.; Grange, S.; Belinga, C.; Bertrand, E.; Duccini, J.C.; Faye, C.; Daudeville, L. Experimental analysis of a shake table test of timber-framed structures with stone and earth infill. *Earthq. Spectra* **2017**, *33*, 1075–1100. [CrossRef]
40. SAP2000. Integrated Software for Structural Analysis and Design. Computers and Structures Inc., Berkeley, California. Available online: https://www.csiamerica.com/products/sap2000 (accessed on 24 October 2024).
41. Huang, Z.; Cheng, Y.; Zhang, D.; Yan, D.; Shen, Y. Seismic fragility and resilience assessment of shallowly buried large-section underground civil defense structure in soft soils: Framework and application. *Tunn. Undergr. Space Technol.* **2024**, *146*, 105640. [CrossRef]